esteem3

Enabling Science through European Electron Microscopy

Second report on TEM methods applied to materials for energy

Deliverable D8.2 – version 1

Estimated delivery date: M36 December 2021

Actual delivery date: M36 December 2021

Lead beneficiary: CAD, JSI

Person responsible: Susana Trasobares and Miran Ceh

Deliverable type: ☒ R ☐ DEM ☐ DEC ☐ OTHER ☐ ETHICS ☐ ORDP

Dissemination level: ☒ PU ☐ CO ☐ EU-RES ☐ EU-CON ☐ EU-SEC

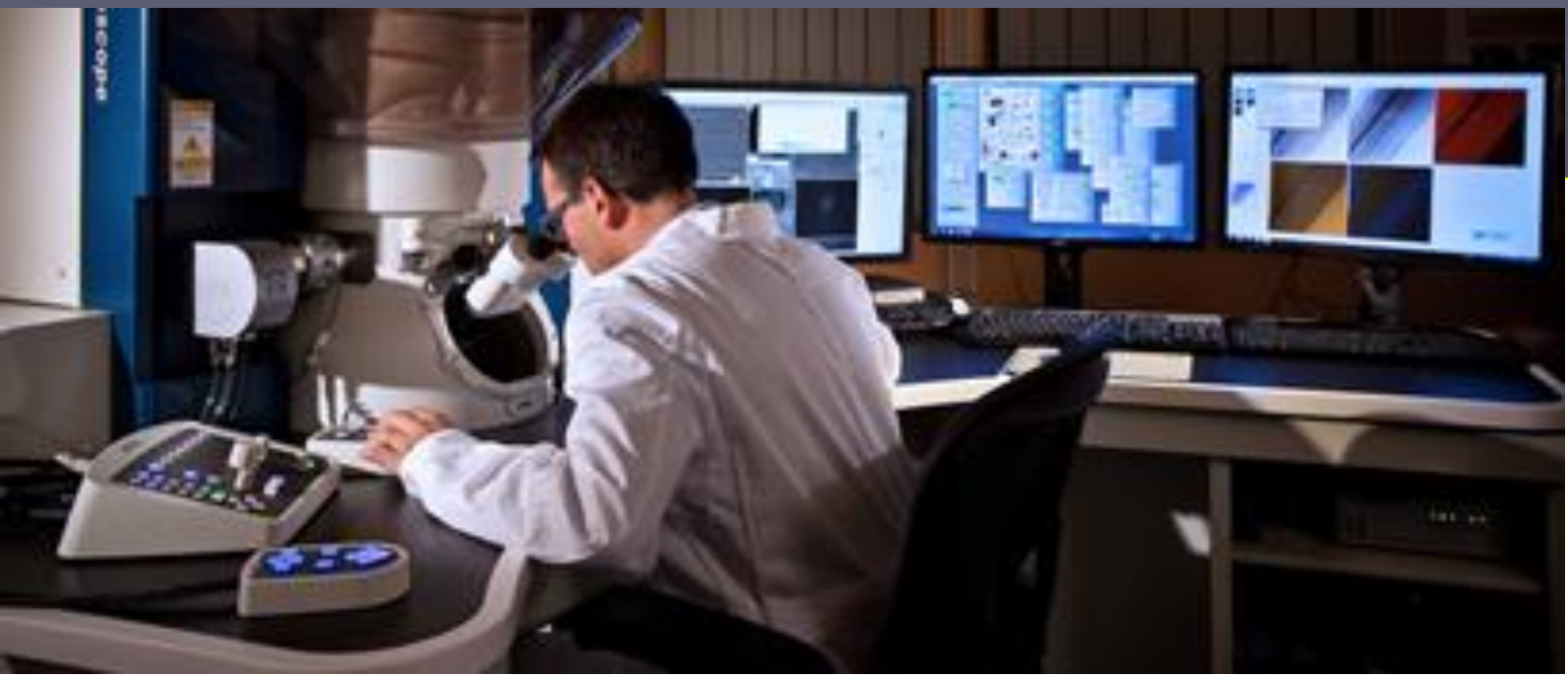

THIS PROJECT HAS RECEIVED FUNDING FROM THE EUROPEAN UNION'S HORIZON 2020 RESEARCH AND INNOVATION PROGRAMME UNDER GRANT AGREEMENT NO **823717**

Grant Agreement No:	823802
Funding Instrument:	Research and Innovation Actions (RIA)
Funded under:	H2020-INFRAIA-2018-1: Integrating Activities for Advanced Communities
Starting date:	01.01.2019
Duration:	54 months

Table of contents

Revision history log

Version number	Date of release	Author	Summary of changes
V0.1	01.12.2021	M. Čeh	Draft version of the deliverable
V0.1	03.12.2021	Peter A. van Aken	Approval of document
V1	03.12.2021	Aude Garsès	General review

Context of the present report

Quoted from the proposal:

"Spectroscopy and imaging techniques for quantitative structural and chemical characterization of materials will be applied to a range of energy materials. This WP will use in-situ capabilities to perform dynamic characterisation of materials for energy and will develop sample preparation recipes specific to these systems, including the key issue of anaerobic sample environments for new battery materials".

Deliverable D8.1 belongs to WP8 Materials for Energy. In this work package four different task have been included. Here in we will describe the progress carried out in every task after Deliverable 8.2.

Task 8.1 Nanomaterials for Sustainable Development

1. ZnO nanostructures

The characterization of optically active defects in ZnO nanorods subjected to thermal annealing in different environments (O_2 and Ar) has been performed by means of STEM-HAADF imaging and XEDS (Fig. 1) showing no appreciable changes in the distribution of the elements in the areas with pores or bubbles with respect to the rest of the material, regardless of the environment (inert or oxidizing) used. (Collaboration between CAT and CAD).

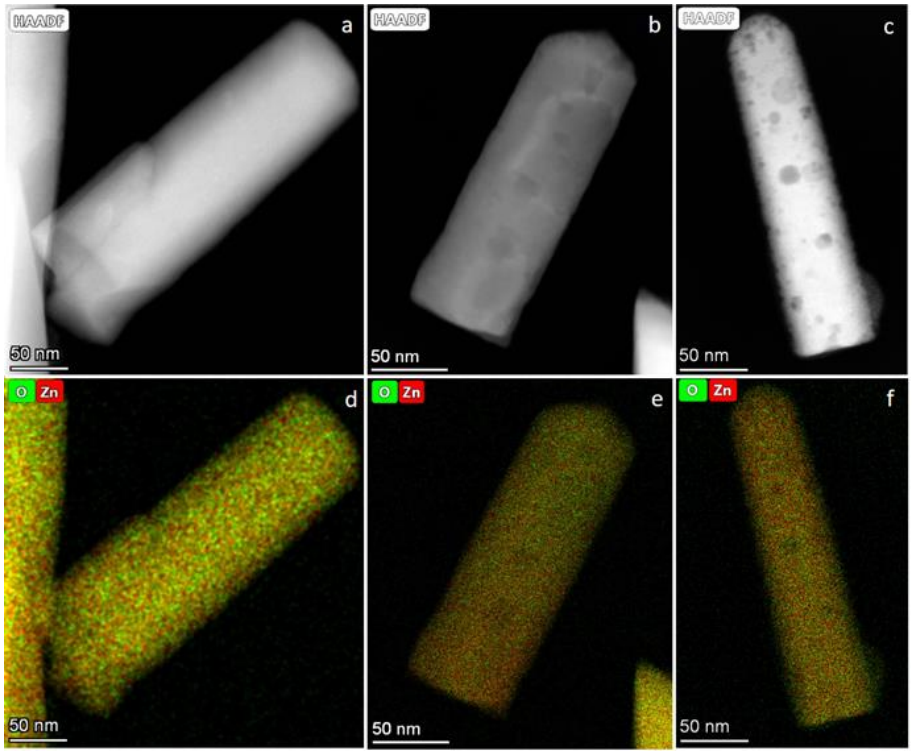

Figure 1. HAADF STEM images and XEDS maps of ZnO nanorods without annealing (a,d), after O2 annealing (b,d) and after Ar annealing (c,f) acquired in Talos microscope of SCCYT UCA.

2. TEM and DFT Study of Basal-plane Inversion Boundaries in SnO_2-doped ZnO

Using atomic resolution scanning transmission electron microscopy (STEM) methods we confirmed that in SnO_2-doped ZnO the IBs form in head-to-head configuration, where ZnO_4 tetrahedra in both ZnO domains point towards the IB plane composed of a close-packed layer of octahedrally coordinated Sn and Zn atoms (Fig. 2). The in-plane composition is driven by the local charge balance, following Pauling's principle of electroneutrality for ionic crystals, according to which the average oxidation state of cations is 3^+. To satisfy this condition, the cation ratio in the IB-layer is Sn^{4+}:Zn^{2+} = 1:1. This was confirmed by concentric electron probe analysis employing energy dispersive spectroscopy (EDS) showing that Sn atoms occupy 0.504 ± 0.039 of the IB layer, while the rest of the octahedral sites are occupied by Zn. IBs in SnO_2-doped ZnO occur in the lowest energy, IB_3 translation state with the cation sublattice expansion of $\Delta IB_{(Zn–Zn)}$ of +91 pm with corresponding O-sublattice contraction $\Delta IB_{(O–O)}$ of –46 pm. Based on quantitative HRTEM and HAADF–STEM analysis of in-plane ordering of Sn and Zn atoms, two types of short-range distributions were identified, (i) zigzag and (ii) stripe. Density functional theory (DFT) calculations showed that the energy difference between the two arrangements is small (~6 meV) giving rise to their alternation within the octahedral IB layer. As a result, cation ordering intermittently changes its type and the direction to maximize intrinsic entropy of the IB layer is driven by the in-plane electroneutrality and 6-fold symmetry restrictions. A long-range in-plane disorder, as shown by our work, would enhance quantum well effects to phonon scattering, while Zn^{2+} located in the IB octahedral sites would modify the bandgap, and enhance the in-plane conductivity and concentration of carriers.

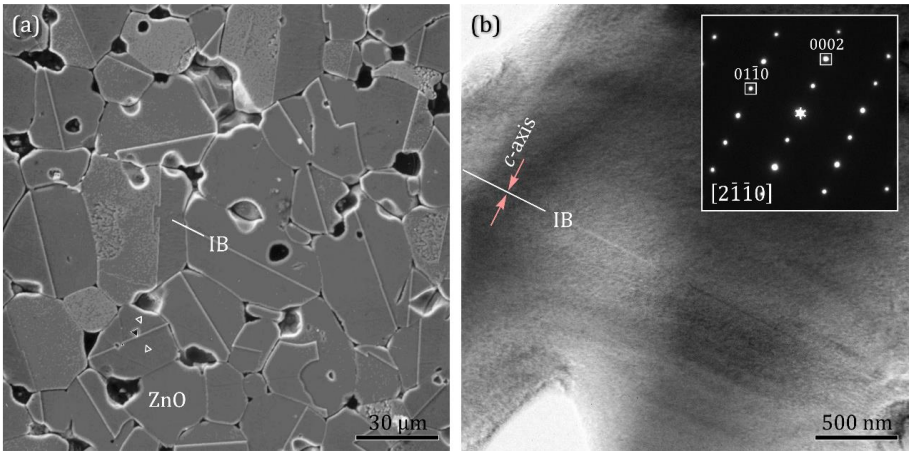

Figure 2. Inversion boundaries (IB) in SnO_2-doped ZnO. (a) SEM image of ZnO–1mol% Bi_2O_3 ceramics doped by 0.1 mol% of SnO_2. After short etching of polished microstructure in dilute HCl the IBs appear as straight planar defects in ZnO grains. Triangular etch pits are pointing towards the IB-plane. (b) BF-TEM image of IB in SnO_2-doped ZnO with a corresponding selected area electron diffraction pattern in [21-1-0] projection, indicating that IBs lie in basal planes of ZnO structure.

Figure 3 shows a typical HAADF-STEM image of the Sn-rich IB in [21-1-0] projection with easily identifiable cation stacking across the IB plane. The cation stacking in the Sn-rich IB corresponds to the lowest energy IB3 translation, having the largest fraction of hexagonal bonds (*wow*). The stacking sequence corresponds to Aβ–Bα–AβC–γB–βC (with cation sites denoted by Greek, and anion sites by Latin letters), suggesting that IB3 is likely to be the only stable IB configuration in SnO_2-doped ZnO [1].

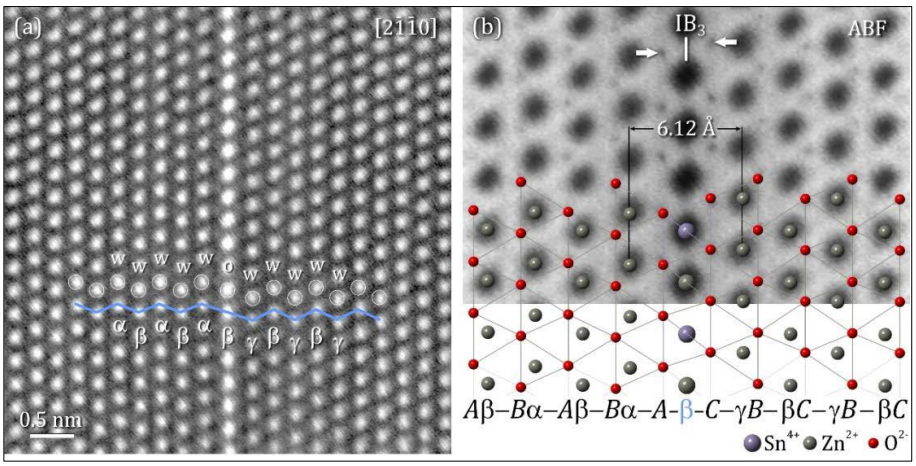

Figure 3. High-resolution STEM images of the Sn-rich IB in [21-1-0] projection. (a) HAADF-STEM image displaying a higher contrast for atomic columns along the IB-plane. Cation positions facilitate a direct identification of IB translation. (b) ABF-STEM image showing the positions of O-columns (weak dark dots). These assist us to identify the coordination of cations and the type of polarity inversion. Below is overlaid DFT relaxed model of the Sn-rich IB (stripes variant of cation distribution) with a stacking sequence of IB_3 translation.

3. Development of 2D materials-based heterostructures for photocatalysis

Since the last two years, CAD is working on the characterization of various photocatalytic devices, in particular applied on the removal on pollutants and on the production of clean energy. In this regard, the use of advanced transmission microscopy techniques is an important part of the project as it allows us to derive without ambiguity the structure-property relationship, which is necessary for the rational design of our catalysts. In particular, we have developed several catalysts based on graphene, which are showing promising results for the removal of various indoors and outdoors toxic substances including benzene and nitrogen oxides gases. The combination of HRTEM and monochromated EELS highlighted that the pH of the synthesis has a strong impact on the crystalline quality and sp^2 fraction of the graphene flakes (Fig. 4). We highlighted the exceptional characteristics of the TiO_2/graphene hybrid material synthesized with 1.0 wt% graphene, and its excellent suitability for multi-purpose applications in the field of environmental remediation. Compared to unmodified titania, it showed a clear enhancement in the photocatalytic removal of those hazardous pollutants (Fig. 5), having a photocatalytic degradation rate twice higher. In addition, the same material was highly stable and showed fully recyclability over repeated tests [2].

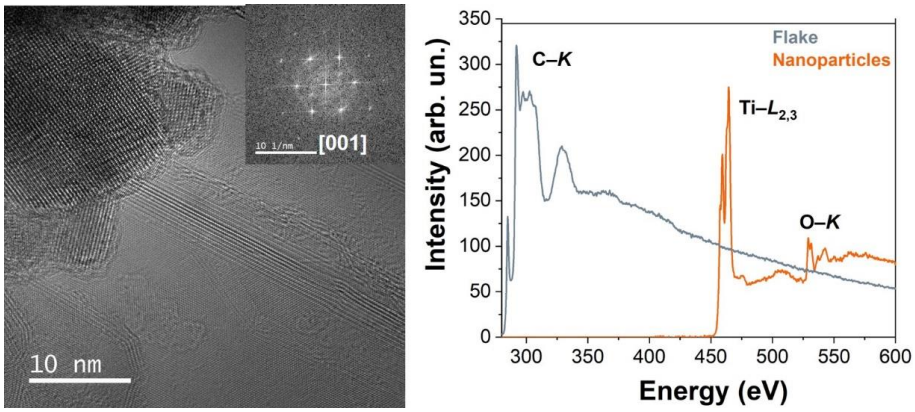

Figure 4. (left) HRTEM image obtained on the graphene-TiO_2 hybrid nanostructures, (right) corresponding monochromated EELS spectra.

On the other hand, sol-gel synthesis performed in more acidic conditions led to an important degradation of the crystalline quality of the graphene flakes. In particular, we have shown by using EELS that strong acidic pH led to the formation of graphene oxide with about 50% of atomic concentration of oxygen. While this material did not show a great effectiveness on the removal of pollutants, it showed a very strong activity for the photocatalytically assisted generation of H_2 under UV irradiation. In particular, it granted a two-fold increase in hydrogen production compared with that of unmodified titania, allowing thus to increase notably the production rate of green hydrogen [3].

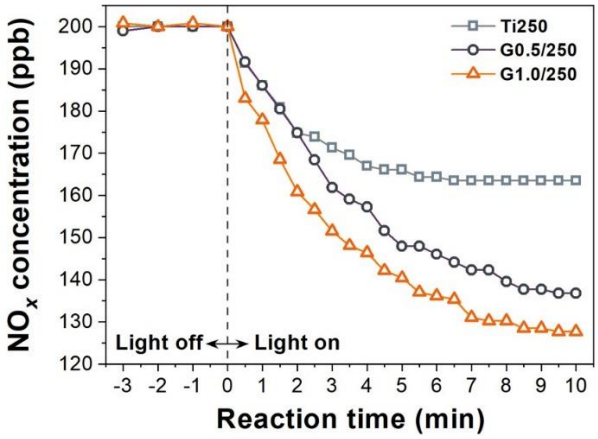

Figure 5. Photocatalytic removal of nitrogen oxide gases upon simulated solar illumination.

4. 2D materials for electrocatalysis

Another important aspect of our work lies in the synthesis and characterization of 2D-based materials for pure electrocatalysis applications. Most of our work is focused on the hydrogen evolution and CO_2 reduction reactions (CO2RR). CO2RR under ambient conditions, which can be coupled with renewable electricity sources, represents a promising approach to reuse the CO_2 emissions, while generating value-added fuels and chemicals. Starting from the graphitization of Ni-based metal organic framework, we were able to synthetize single-atom nickel catalysts (SAC) on two-dimensional nitrogen-doped carbon nanosheets. In particular, by combining TEM (Fig. 6) with XPS and XAS, we highlighted the SAC nature of the catalyst. The SAC catalysts reached high performance activity and energy efficiencies as high as 85% at j_{CO}= 7.2 mA cm^{-2} [4].

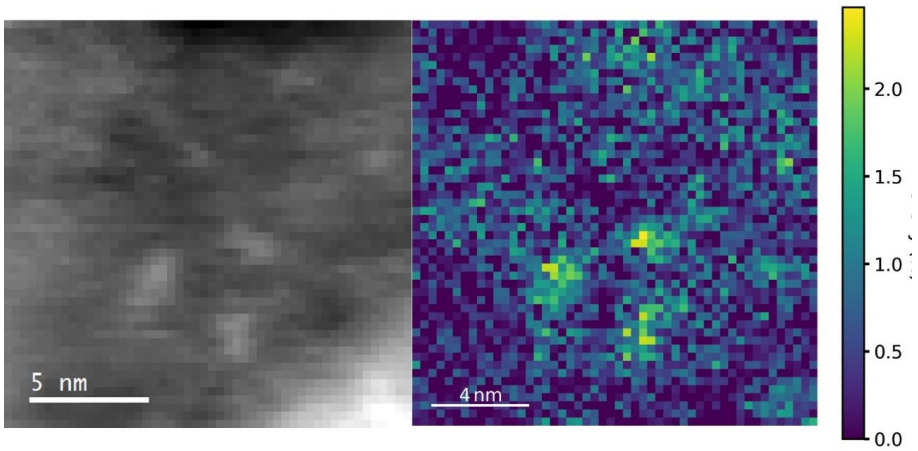

Figure 6. (left) ADF image acquired on the carbon sheet (right) Ni at. % map derived from EELS measurements.

5. Oxygen evolution on beam sensitive energy nanomaterials based on hollandite and ceria

Using an alternative approach to determine the z-factors (developed within WP5 Task 5.3: Increasing accuracy and reproducibility through correlation and coincidence experiments), the phase transformation from fluorite type CeO2 to the cubic sesquioxide, Ce_2O_3, phase has been tracked by exposing the sample to the electron beam. In particular, the evolution of Ce-L and O-K lines has been followed by EDS in chrono-spectroscopic mode. The quantification by using z-factors clearly shows that at% of O varies from 66% to 60% after 45 min (Fig. 7). This change in the O at% is in agreement with a transformation in which Ce oxidation state evolves from Ce^{+4} to Ce^{+3}.
The effect of the electron beam in this system has already been studied by EELS, however, to the best of our knowledge this is the first time that quantitative information about oxidation state is obtained using EDS. Moreover, this approach opens the possibility of using EDS to unveil details of the redox chemistry of cerium oxide based materials, with subnanometer spatial resolution, by performing in-situ experiments in which the redox potential and temperature of the environment can be properly controlled.

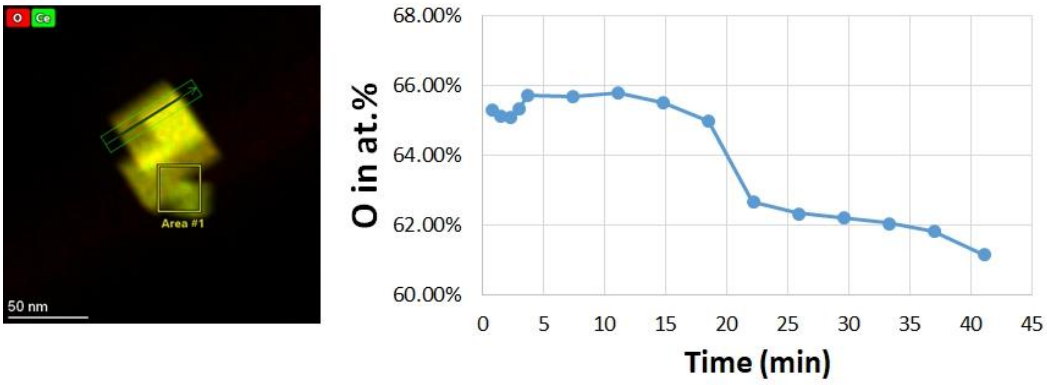

Figure 7. EDS elemental map of CeO_2 (left) and quantification of O in at. % as a function of the time (right).

Task 8.2 Dynamic Characterization of Energy Materials

Dynamic characterization of energy materials are performed using in-situ capabilities available in WP6.

1. *In-situ* LC TEM of Ni deposition from aqueous solutions

Electrochemical nucleation and growth of nickel from aqueous solutions was studied by *in-situ* LC-TEM. A series of different electrochemical experiments were performed going from conventional and ex-situ electrochemical experiments to final in-situ LC-TEM experiments in the TEM. By carrying out these experiments it was possible to evaluate crucial parameters that affect nucleation and growth of metal nickel on platinum working electrodes, as well as to determine experimental conditions of electrodeposition that yield specific morphologies of nickel such as isolated dendritic nanostructures and/or solid films. This is highly relevant, especially for the applications of electrochemically prepared metallic sensors for various applications, where the surface morphology is of utmost importance.
The *in-situ* TEM experiments confirmed that it is highly important to control the electron dose during the experiments. At a high dose rate, corresponding to 46000 e/nm^{2}s, the nucleation, and growth of nickel was a combination of radiolytic species effect in water and electrodeposition (Fig. 8). The electrochemical dissolution on the other hand showed that nickel can be reduced even at this high

electron dose thus proving the reversibility of the process. At a low flux of 1300 e/nm^{2}s, the water radiolysis effect was negligible and the electrochemical deposition was the main mechanism for Ni reduction from the aqueous solution. However, it was observed that the morphology of Ni deposits largely depended on the concentration of Ni solution. When using 1 mM solution, the Ni deposits exhibited dendritic growth resulting in isolated Ni nanostructures with a high surface. At higher 5 mM concentrations the Ni grew in uniform films (Fig. 9). The thickness measurement of deposited Ni films during the growth showed that the growth of the Ni films was linear with the time during the first 60 s of the deposition (Fig. 10) [5].

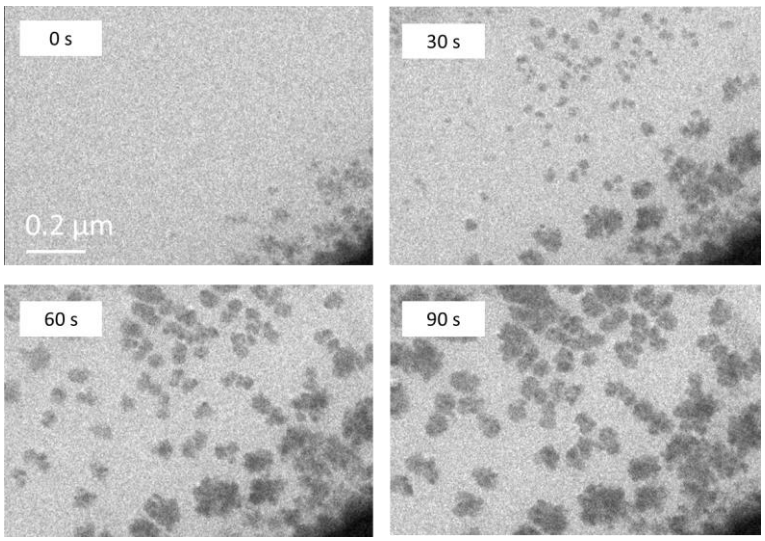

Figure 8. Beam-induced nucleation and growth at high dose 5·10^7 e/nm^2 for one experiment (100s) at CA -0.2 V using 5 mM $NiSO_4$.

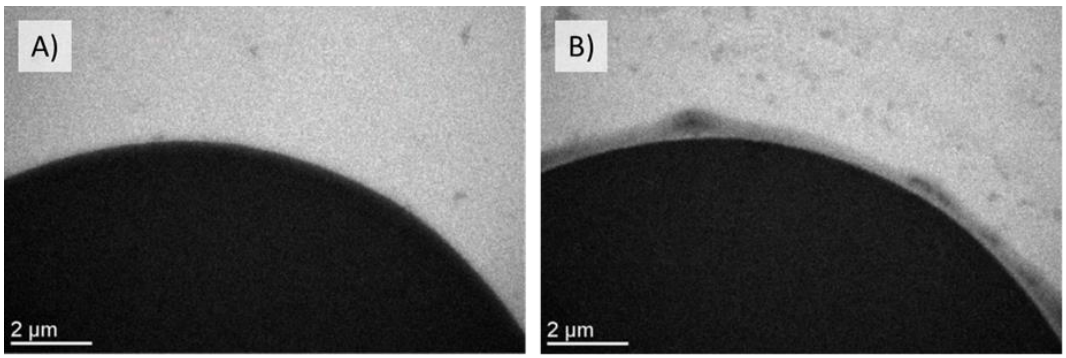

Figure 9. Electrochemical nucleation and growth for 5 mM $NiSO_4$. A) The Pt electrode before the applied potential. B) After the electrodeposition at a constant potential -1.5V.

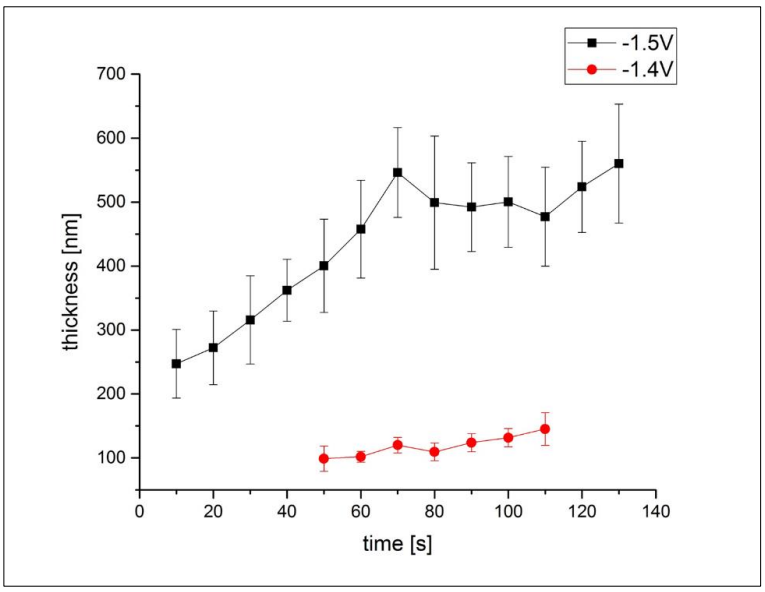

Figure 10. Growth evaluation of two depositions using 5 mM Ni_2SO_4.

Task 8.3: Characterization of Devices for Energy Applications

1. Establishing the relationship between time and oxidizing environment on the oxide scale formation on ATI 718Plus® superalloy

ATI 718Plus® superalloy (718Plus) is a polycrystalline nickel-based superalloy with enhanced high-temperature capabilities compared to the well-known Inconel 718 superalloy. Due to changes in chemical composition, its maximal application temperature was increased from 650 °C to 700 °C, compared to its predecessor. One of the critical characteristics of nickel-based superalloys is the ability to withstand operation in harsh environments, such as CO_2 and NO_x gases, for more than 100.000 hours at elevated temperatures.

The study aimed to establish a correlation between the oxide scale formation on 718Plus superalloy and different oxidation parameters, such as environment and time. Oxidation tests were performed at a constant temperature of 850 °C. In the present study, the evolution of the oxide scale and near-surface microstructure in 718Plus superalloy was investigated using analytical electron microscopy combined with FIB-SEM tomography.

Longer oxidation duration led to the formation of a thicker external oxide scale and deeper internal oxidation zone of 718Plus superalloy. The outer oxide scale was formed mainly of Cr_2O_3, with some amount of other oxides, such as TiO_2. The thickness of the oxide scale increased from about 2 µm after oxidation for 120 hours to 10 µm after 4000 hours of oxidation. In the internal oxidation zone, Al_2O_3 were formed mainly at the grain boundaries due to favourable elements diffusion conditions. Figure 11 presents FIB-SEM tomographic reconstruction of the internal oxidation zone from the top view throughout the external oxide scale. Here, the formation of alumina at the grain boundaries is clearly visible and was accompanied by the intermetallic δ-Ni_3Nb phase. The depth of this zone increased with time as well, from about 5 µm after 120 hours to almost 20 µm after 4000 hours.

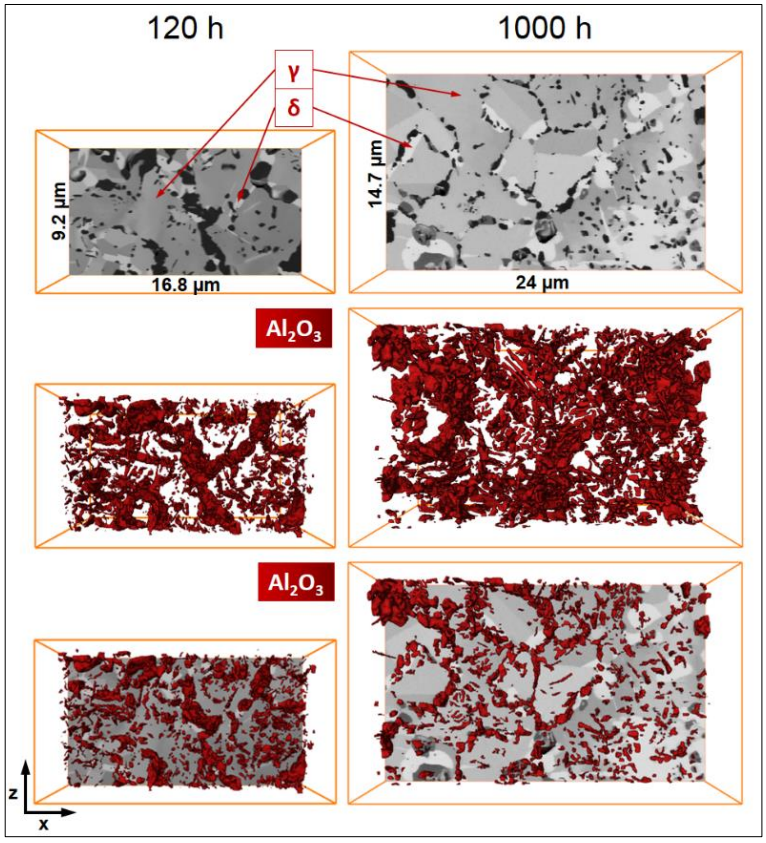

Figure 11. 3D tomographic reconstruction of the distribution of the Al_2O_3 phase: A) top view; B) top view with an orthoslice inserted at the depth of 7 µm from the top; C) the orthoslice used to generate image 1B.

The STEM analysis of the oxide scale revealed some nanometric particles present within it. We found that those were non-oxide, metallic particles containing Ni, Co, and Fe, so γ phase forming elements. Moreover, the particles were precipitated from the chromia instead of getting trapped inside during the grain growth. For the sample oxidized in laboratory dry air, the particles were found after a longer oxidation duration. However, for samples oxidized in laboratory air containing 10 vol.% of water vapour, similar particles were found after only 120 hours of oxidation. Figure 12 presents a high-resolution STEM analysis of interfaces between δ-Ni_3Nb, γ-Ni and Cr_2O_3 phases present in the oxide scale of 718Plus superalloy. Figure 12a shows a STEM-HAADF image of the scale and the area underneath, highlighting the presence of δ phase particles in this area (Figure 12b). The HRSTEM-HAADF imaging revealed columns of δ-Ni3Nb phase atoms (Figure 12c). A JEMS-simulated HAADF image of the same δ-Ni_3Nb arrangement is superimposed onto the image in this figure (highlighted in blue). In contrast, the fast Fourier transform (FFT) of this image is shown in the rightmost part of this figure. The HAADF image calculated for this orientation matched the experimental high-resolution image (Figure 12c). The bright and dark spots observed in the δ-Ni_3Nb phase correspond to Nb and Ni, respectively. Figure 12d shows superimposed STEM-EDXS maps of selected chemical elements, and these maps confirm the chemical and crystallographic complexity of the particle shown in Figure 12b. Figure 12e presents FFT images for the γ and δ-Ni_3Nb phases as well as their superimposition, from which it follows that the g_γ = [1−1−1] and g_δ = [400] reflections are very close, indicating that the interplanar distance between the $\{111\}_\gamma$ and $\{004\}_\delta$ crystallographic planes is small. Figure 12f shows the HRSTEM-HAADF image of the δ-Ni_3Nb precipitate and the γ matrix atom columns. The rightmost small figures present a HAADF image of the γ phase nanostructure and its image simulated by JEMS (highlighted in blue) as well as an FFT for this phase.

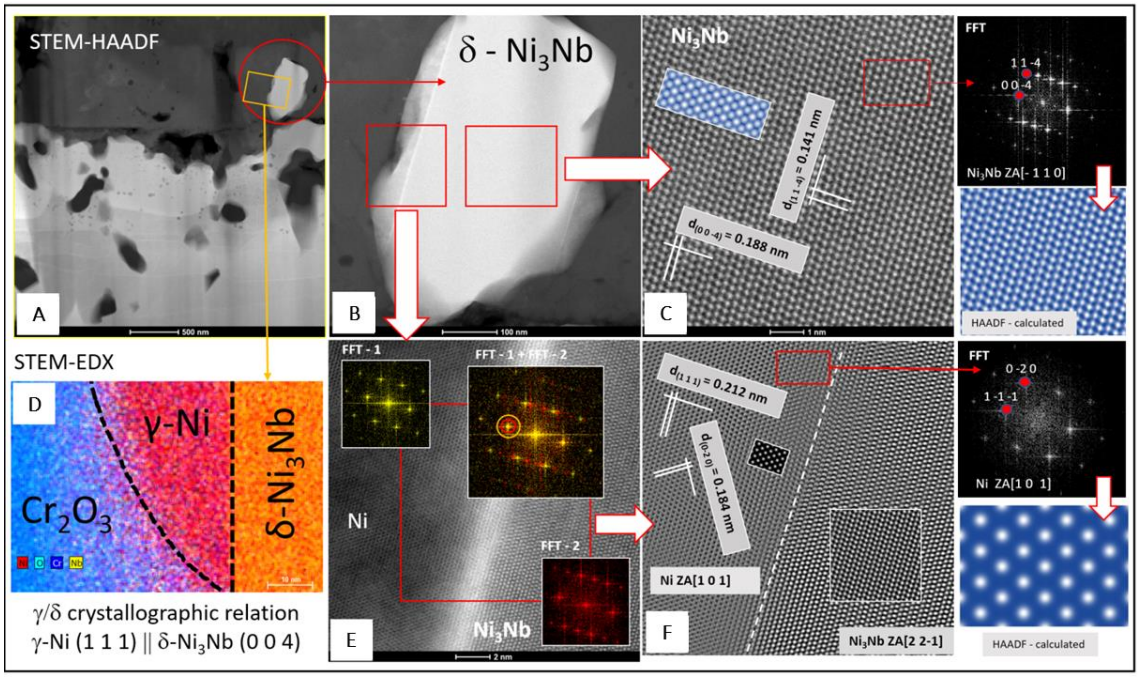

Figure 12. High-resolution analysis of δ phase observed in the scale layer formed on the 718Plus superalloy after oxidation at 850 °C for 120 h in wet air: (a) STEM-HAADF image of the scale and beneath highlighting the presence of δ-Ni_3Nb particle particles in this area Figure (b), (c) HRSTEM-HAADF image of a δ-phase particle with FFT image and HAADF image simulated using JEMS software, (d) superimposed STEM-EDX maps of selected elements, (e) FFT analysis of selected areas of HRSTEM-HAADF image, and (f) HRSTEM-HAADF image after filtering using an FFT showing the δ-Ni_3Nb/γ interface.

Lastly, we identified and described the formation of the intermetallic δ-Ni_3Nb interlayer. It was formed between the outermost chromia scale and bulk material of 718Plus superalloy. Due to application of FIB-SEM tomography, we revealed that it is in fact a discontinuous layer, where a significant amount of holes was observed. In the tomographic reconstruction, these holes were filled with either Cr_2O_3 or Al_2O_3 oxides. Chemical analysis of the δ phase by STEM-EDXS, confirmed a low solubility of other elements within it. Thus, it was concluded that holes present within this layer are the only paths to transport chromium, from bulk material into the chromia scale, and for oxygen to diffuse into the bulk material/internal oxidation zone. This provides new insight into the role of intermetallic layers, as diffusion barriers during oxidation. Figure 13 shows 3D tomographic reconstruction of δ phase interlayer formed in 718Plus superalloy oxidized for 120 hours in laboratory dry air. A so-called orthoslice was inserted directly beneath the δ layer to highlight its discontinuous nature.

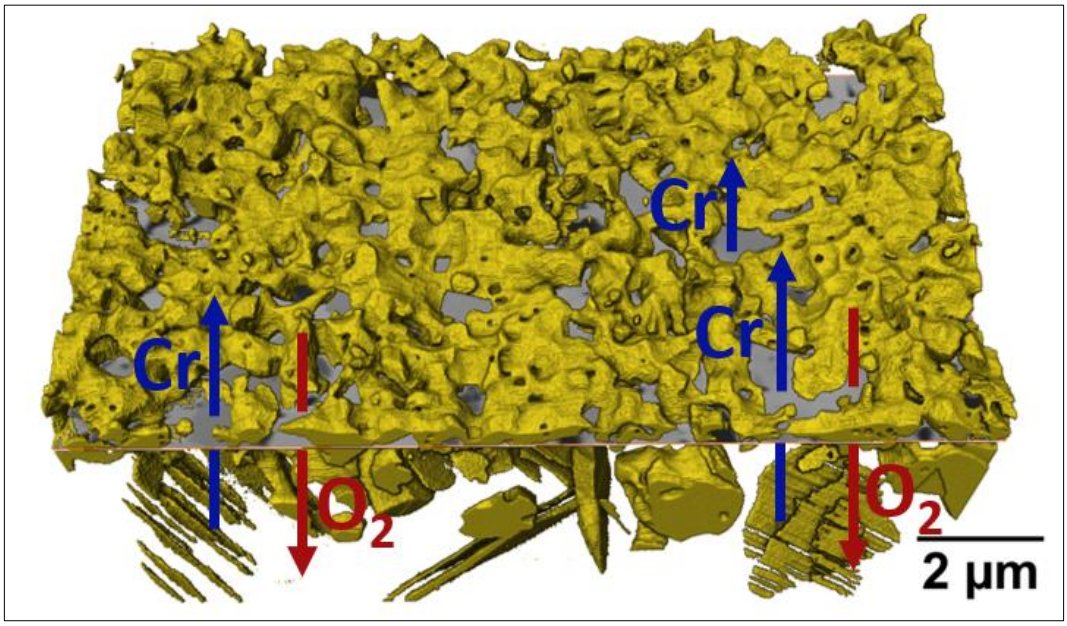

Figure 13. 3D tomographic reconstruction of the δ phase interlayer formed in 718Plus superalloy after 120 hours oxidation in laboratory dry air.

Detailed analysis of the influence of the oxidation time on the oxide scale formation of 718Plus superalloy can be found in the article published in *Corrosion Science* [6], while the description of the relationship between oxide scale formation and the oxidizing environment was published in *Materials* [7]. Formation and role of the δ phase interlayer was most extensively described in *Scripta Materialia* [8].

2. Multimodal discontinuous reaction in Ni-Fe-Cr-Al alloy

Haynes HR-224 is a wrought Ni-Fe-Cr-Al alloy with a superior oxidation resistance and potential application in energy-related industries. During ageing treatment, between 600-900 °C discontinuous precipitation (DP) zone was formed at the grain boundaries. In this study, SEM, TEM and STEM-EDXS were applied to explore the relationship between the occurring grain boundary precipitation phenomena and mechanical behaviour. Within the discontinuous precipitation zone, three different phases were recognized, namely γ solid solution with lamellar $M_{23}C_6$ carbides and elongated γ' precipitates at the reaction front. Coherency of the discontinuous precipitates was identified, as they have shown a cube-on-cube orientation relationship. Furthermore, the development of multiple discontinuous reactions was discussed. Figure 14 shows TEM analysis of discontinuous precipitation in HR-224 alloy aged for 2 hours at 700 °C. Initially, the dual-phase nature of the DP was recognized, where parallel precipitates of $M_{23}C_6$ carbides were present in the γ matrix. These carbides were observed at the dislocation boundary formed between the DP zone and original, as indicated by yellow dashed lines (Fig. 14b). A selected area diffraction pattern (Fig. 14c) was solved for γ, γ' and $M_{23}C_6$ phases in a [1 1 2] zone axis, as shown in Fig. 14d. The red circle in the SAED pattern shows the spots used to obtain the TEM dark-field (TEM- DF) image (Fig. 14e). All four spots within the circle correspond to $M_{23}C_6$ carbides, demonstrated as bright precipitates at the dislocation boundary and as lamellar precipitates within the DP.

Figure 15a shows a STEM-HAADF image of DP along with STEM-EDXS elemental maps of Ni, Cr, Fe and Al. The STEM-EDXS results show a clear separation between three phases at the reaction front, where preferential partitioning of Ni, Cr and Fe was observed. To highlight the separation between three phases, an overlayed map of Ni, Fe and Cr was shown in Fig. 15b, where a dashed arrow indicates the

linescan shown in Fig. 15c. The Cr-rich regions correspond to the precipitation of lamellar $M_{23}C_6$ carbides, which were present across the DP zone. Furthermore, lamellar $M_{23}C_6$ carbides were surrounded by either Ni- and Al-rich zones or Fe-rich zones at the reaction front, indicating the presence of elongated γ' precipitates alternated by precipitation free zones. The intensity of STEM-EDXS elemental maps suggests a low solubility of both Ni and Fe in $M_{23}C_6$ carbides and moderate presence of Ni in γ solid solution and Fe in γ' phase, which was confirmed by the linescan shown in Fig. 15c. Furthermore, the highest concentration of Al was present in the γ' phase. Complementing, Cr presented a low solubility in the γ' phase and a moderate one in the γ phase. More about this study can be found in article in *Scripta Materialia* [9].

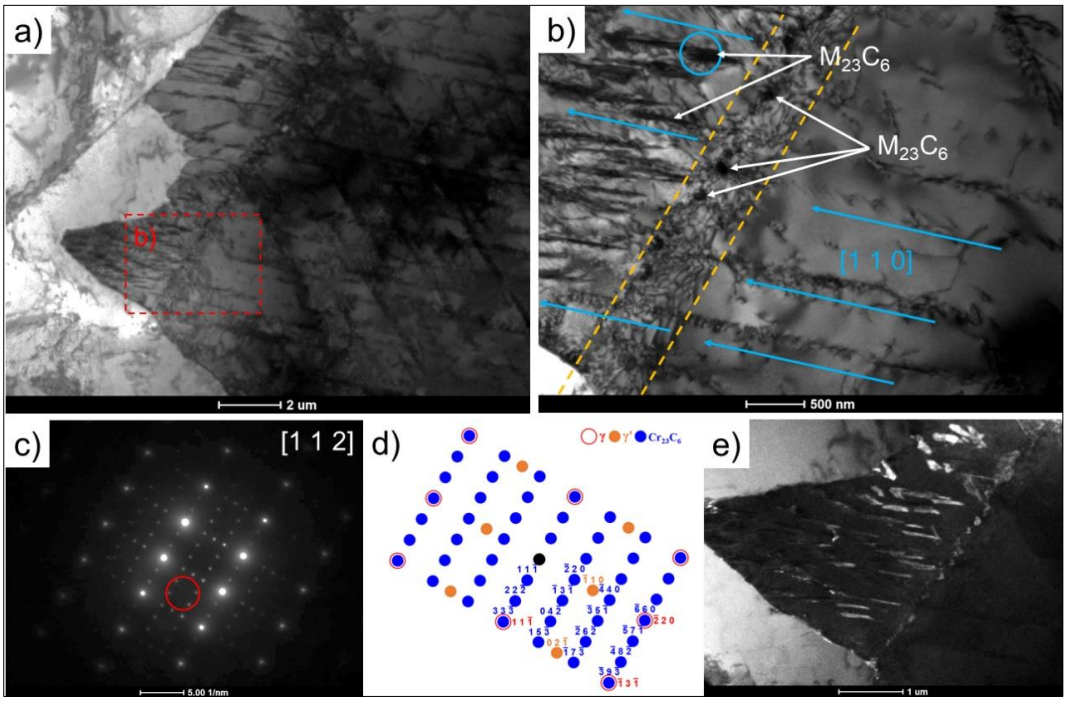

Figure 14. (a) Discontinuous precipitation at the grain boundary in HR224 alloy aged for 2 hrs at 700 °C (TEM-BF); (b) highlighted area at the dislocation boundary indicated by the dashed box in Fig. 14a (TEM-BF); (c) selected area electron diffraction pattern taken from the area marked with a blue circle in Fig. 14b; (d) solution for diffraction pattern present in Fig. 14c; (e) TEM-DF image of $M_{23}C_6$ carbides in discontinuous precipitation, aperture position for DF imaging was indicated by the red circle in Fig. 14c.

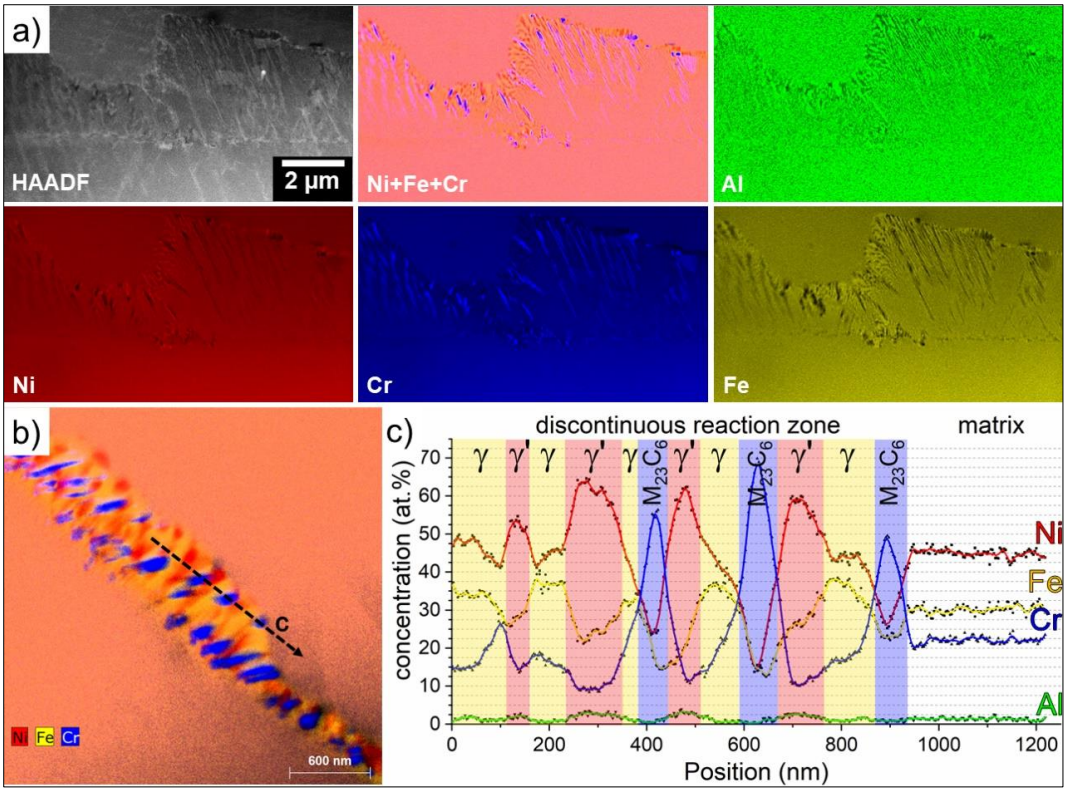

Figure 15. (a) STEM-HAADF image of discontinuous precipitation at the grain boundary in HR224 alloy aged for 2 hrs at 700 °C with corresponding STEM-EDXS distribution maps of selected elements.; (b) overlayed STEM-EDXS elemental distribution map of Ni, Cr and Fe of discontinuous precipitate at the grain boundary in HR224 alloy aged for 2 hrs at 700 °C. ; (c) EDXS linescan of element distribution acquired.

3. Dry reforming of methane over $Ni/Ce_{0.8}Ti_{0.2}O_{2-\delta}$

Dry Reforming of Methane (DRM) reaction (CH4 + CO2 ↔ 2CO + 2H2) has recently attracted the interest of both academia and industry. DRM is a highly endothermic reaction (ΔHo = +261 kJ mol^{-1}) suitable for the utilization of both Natural Gas (NG) in gas fields consisting of high concentrations of CO_2 (> 40 vol%) and renewable Biogas (use of biowastes as feedstock) towards syngas (H_2/CO) and hydrogen (green fuel) formation for electricity generation in fuel cells. The derived synthesis gas consisting of a favourable ratio of H_2/CO ~ 1 can also be used for the production of liquid fuels and other chemicals (DME, MeOH and Acetic Acid). The simultaneous utilization of two major greenhouse gases (CH_4 and CO_2) mitigates global warming. The effects of Ni particle size (d_{Ni} ~ 22–45 nm) of $Ni/Ce_{0.8}Ti_{0.2}O_{2-\delta}$ on the carbon paths in the dry reforming of methane at 750 ◦C have been investigated by various transient and isotopic experiments as well as TEM. The crystal structure and phase composition of the $Ce_{0.8}Ti_{0.2}O_{2-\delta}$ – supported Ni catalysts and the Ni particles morphology and size distribution were analysed by transmission electron microscopy (Fig. 16). For Ni particle size (Feret diameter, nm) distribution, a number of Ni particles of 230 (3 wt% Ni), 810 (7.5 wt% Ni) and 1054 (10 wt% Ni) were measured for reducing the statistical mean Ni particle size error estimation (Fig. 17). The Ni metal dispersion (D_{Ni}, %) was estimated based on the TEM analyses results [10].

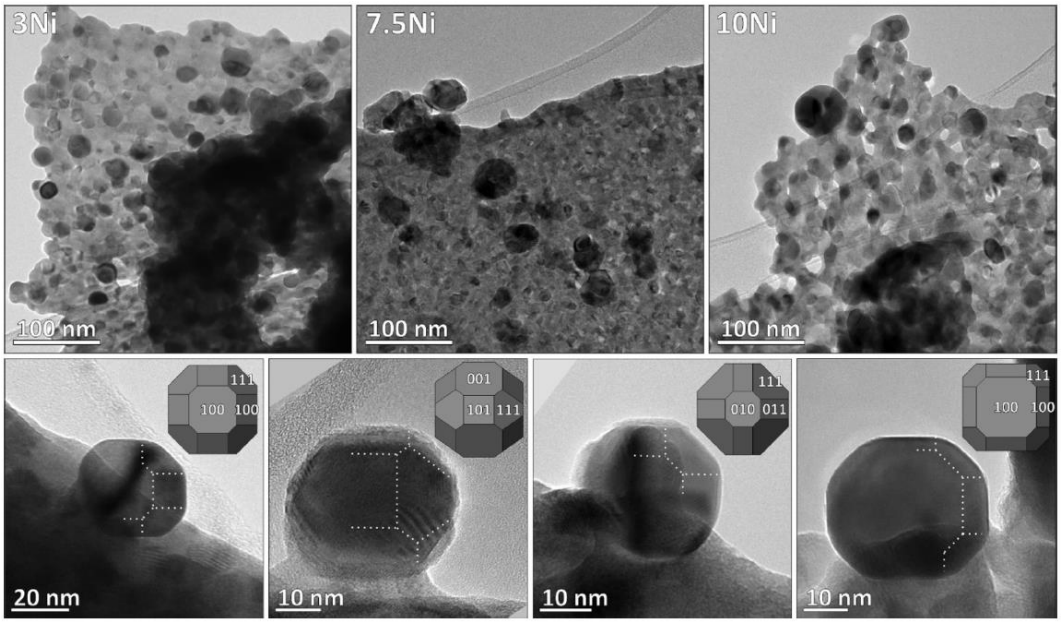

Figure 16. TEM micrographs of $Ce_{0.8}Ti_{0.2}O_{2-\delta}$ supported 3 wt% Ni (3Ni), 7.5 wt% Ni (7.5Ni) and 10 wt% Ni (10Ni) catalysts. Darker truncated particles are Ni nanocrystals, firmly intergrown onto the surface of the Ce-Ti-O plate-like support. The morphology of the Ni nanocrystals is a combination of cube {100}, octahedron {111} and rhombic dodecahedron {110}.

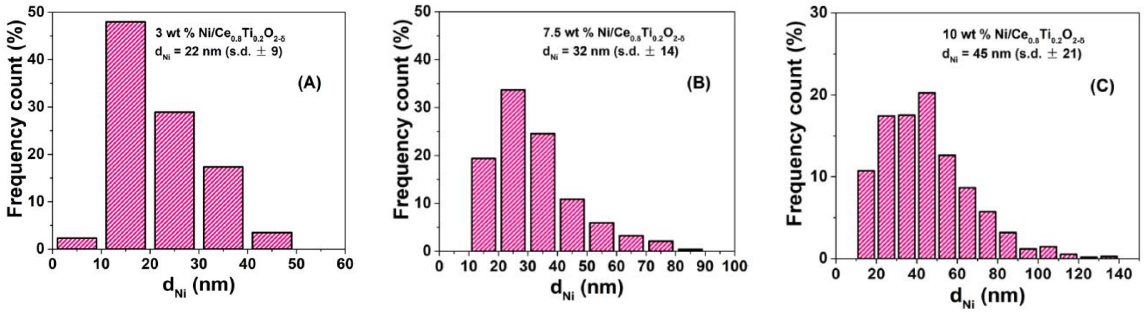

Figure 17. Ni particle size distribution (Feret diameter, nm) for the $Ce_{0.8}Ti_{0.2}O_{2-\delta}$ supported 3 wt% Ni (A), 7.5 wt% Ni (B) and 10 wt% Ni (C) catalysts.

Task 8.4: Sample Preparation of Materials for Energy

Within this task, different methods for TEM sample preparation of materials/devices for energy applications are optimised and implemented.

1. Welds in Al-based alloy

Welding significantly changes the microstructure of metals/alloys. The interface between the normal microstructure and welding area is not abrupt; so the choice and positioning of the FIB lamella is not only difficult, but usually not possible. We used a combination of tripod polishing and ion-milling techniques with special care of positioning the interfacial regions of interest prior to ion-milling (Fig. 18, 19).

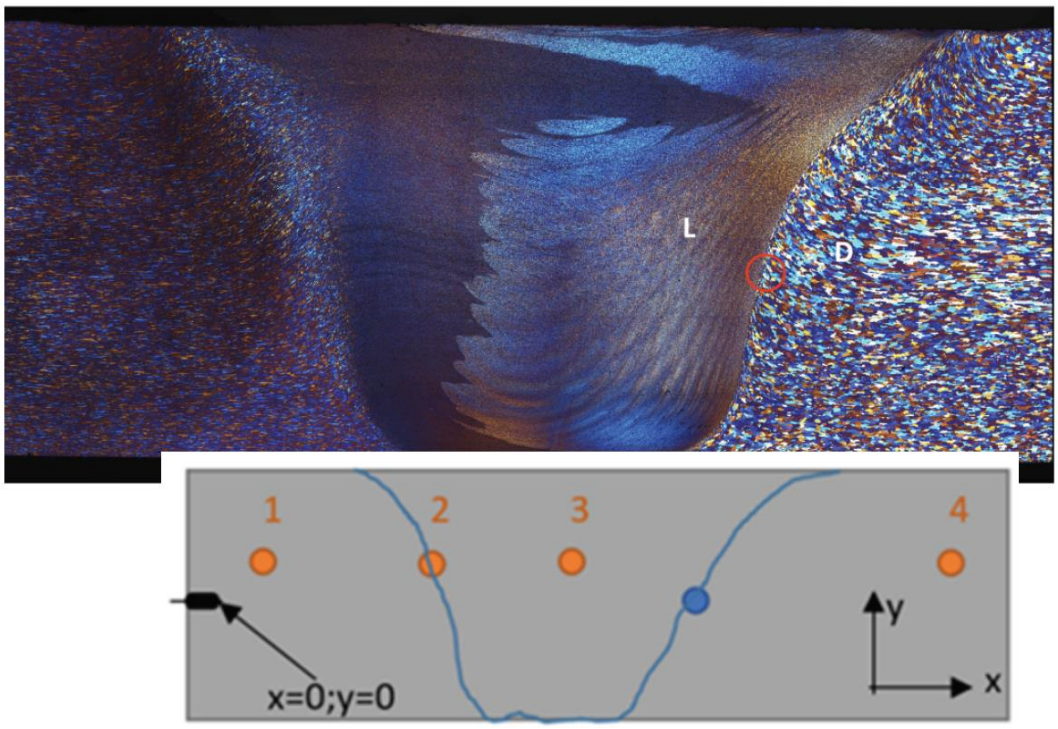

Figure 18. Marked ROIs in the Al-based alloy after welding.

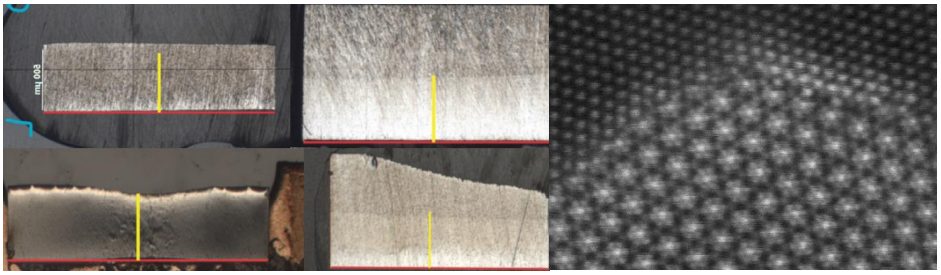

Figure 19. (left) Determination of the interface exact position (right) Interface between L and D(red circle).

REFERENCES

1. Ribić V., Rečnik A., Dražić G., Podlogar M., Branković Z., Branković G., *TEM and DFT study of basal-plane Inversion boundaries in SnO_2-doped ZnO*, Science of sintering, the periodical of the International Institute for the Science of Sintering, 53 (2021) 237.
2. Tobaldi D. M. et al., *Graphene-TiO_2 hybrids for photocatalytic aided removal of VOCs and nitrogen oxides from outdoor environment*, Chemical Engineering Journal, 405 (2021) 126651.
3. Tobaldi D. M. et al., *Cu_XO and carbon–modified TiO_2–based hybrid materials for photocatalytically assisted H_2 generation*, Materials Today Energy, 19 (2021) 100607.
4. Zhang Y. et al., *2.6% cm^{-2} Single-Pass CO_2-to-CO Conversion Using Ni Single Atoms Supported on Ultra-Thin Carbon Nanosheets in a Flow Electrolyzer*, ACS Catalysis, 11 (2021) 12701-12711.
5. Koblar M, In-situ LC-TEM studies of nickel electrodeposition from aqueosu solutions, Master Thesis, Joyef Stefan International Postgraduate School, July 2021.
6. Kruk A., Lech S., Gil A., Cempura G., Agüero A., Wusatowska-Sarnek A.M., Czyrska-Filemonowicz A., *Three-dimensional characterization of an oxide scale on ATI 718Plus® superalloy*, Corros. Sci., 169 (2020) 108634.

7. Kruk A., Gil A., Lech S., Cempura G., Agüero A., Czyrska-Filemonowicz A., *Multiscale Characterization of an Oxide Scale Formed on the Creep-Resistant ATI 718Plus Superalloy during High-Temperature Oxidation*, Materials (Basel), 14 (2021) 6327.
8. Lech S, Kruk A., Gil A., Cempura G., Agüero A., Czyrska-Filemonowicz A., *Three-dimensional imaging and characterization of the oxide scale formed on a polycrystalline nickel-based superalloy*, Scr. Mater., 167 (2019) 16–20.
9. Lech S., Polkowski W., Polkowska A., Cempura G., Kruk A., *Multimodal discontinuous reaction in Ni-Fe-Cr-Al alloy*, Scr. Mat., 194 (2021) 113657.
10. Damaskinos C.M., Zavašnik J., Djinović P., Efstathiou A.M., *Dry reforming of methane over Ni/Ce0.8Ti0.2O2-δ: The effect of Ni particle size on the carbon pathways studied by transient and isotopic techniques*, Applied Catalysis B: Environmental, 296 (2021) 120321.